Check for updates

JGR Solid Earth

RESEARCH ARTICLE
10.1029/2024JB030805

On the Complex Topography of Marine Volcanoes and Its Control on the Spatial and Magnitude Distribution of Surface Displacement

Megan Campbell[1], **Séverine Furst**[1], **Henriette Sudhaus**[2,3], **and Morelia Urlaub**[1,2]

[1]GEOMAR-Helmholtz Centre for Ocean Research, Kiel, Germany, [2]Christian-Albrechts University of Kiel, Kiel, Germany, [3]Karlsruhe Institute of Technology, Karlsruhe, Germany

Abstract Marine volcanoes exhibit significant topographic relief, as they extend from deep below sea level to thousands of meters above. These volcanoes often have complex, asymmetric topographies due to the submersion of their flanks, yet deformation models often approximate this topographic surface as flat and overlook its effect in modeling approaches. This limiting perspective may lead to inaccurate assessments of deformation sources and potential hazards. In this study, we investigate the effect of complete marine volcano topography on deformation modeling. We comprehensively characterize volcano shape by applying a geomorphometric parameterization of natural asymmetry and steepness to describe marine volcanoes. Then, by building upon an existing analytical solution for triangular dislocations, we account for complete edifice topography (from the submarine base to the subaerial peak) and discretized source geometries to be solved in a full-space modeling domain. We demonstrate that models with complex topographies deviate to a greater extent from flat surface models, resulting in significant underestimations of both magnitude (up to 18% and 57% for vertical and horizontal, respectively) and spatial distribution of resultant displacement. In addition, we show that geomorphometric parameterization can provide a first-order approximation of deviation from a model with no topography. In the case of island volcanoes, the resultant displacement field is not confined to the onshore area but can extend beyond the coastline to the submarine edifice. This is particularly important as technology advances and submarine monitoring becomes feasible. Our approach enhances our understanding of volcano deformation scenarios and provides a tool for optimizing GNSS network design.

Plain Language Summary Volcanoes located in marine settings often have greater height than those on land, as they extend from the deep seafloor to high above sea level. This creates complex, asymmetric shapes that can significantly influence deformation models used to understand volcanic activity. In this study, we examine how the complete topography of marine volcanoes, both above and below sea level, affects deformation modeling. By integrating detailed topographic data into an existing computer model, we improve our understanding of how magma movements beneath the surface shape ground motion. We tested this method on marine volcanoes with different shape characteristics: Stromboli and Mount Etna in Italy, and, El Hierro in the Canary Islands. We found that models including the complete topographic surface can be underestimated by traditional models by between 18% and 57% in magnitude and over large areas of the edifice. Additionally, we discovered that ground motion can extend into offshore areas, which are frequently overlooked. Our findings highlight the importance of incorporating full topography into deformation models, particularly as advances in technology make monitoring submerged volcanoes more feasible. This approach could enhance the design of ground motion monitoring systems, improving our ability to detect and respond to volcanic hazards onshore and offshore.

Key Points:

- Marine volcano topography significantly influences surface displacement fields, both in onshore and offshore areas of an edifice
- Geomorphometric parameterization of a marine volcano edifice can provide first-order approximations of deviation from a flat-surface model
- Offshore displacement in marine volcanoes highlights the need for integrated subaerial and submarine monitoring techniques

Supporting Information:

Supporting Information may be found in the online version of this article.

Correspondence to:

M. Campbell,
mcampbell@geomar.de

Citation:

Campbell, M., Furst, S., Sudhaus, H., & Urlaub, M. (2025). On the complex topography of marine volcanoes and its control on the spatial and magnitude distribution of surface displacement. *Journal of Geophysical Research: Solid Earth*, *130*, e2024JB030805. https://doi.org/10.1029/2024JB030805

Received 22 NOV 2024
Accepted 11 AUG 2025

Author Contributions:

Conceptualization: Séverine Furst, Henriette Sudhaus, Morelia Urlaub
Data curation: Megan Campbell
Funding acquisition: Morelia Urlaub
Investigation: Megan Campbell
Methodology: Megan Campbell, Séverine Furst
Project administration: Morelia Urlaub
Software: Megan Campbell
Supervision: Séverine Furst, Henriette Sudhaus, Morelia Urlaub
Visualization: Megan Campbell
Writing – original draft: Megan Campbell, Séverine Furst

© 2025. The Author(s).
This is an open access article under the terms of the Creative Commons Attribution License, which permits use, distribution and reproduction in any medium, provided the original work is properly cited.

1. Introduction

Volcanoes are associated with significant topographic relief and this is especially true for marine volcanoes, which encompass partially submerged edifices partly (coastal) or entirely (island) surrounded by seawater (Furst et al., 2023). Island volcanoes have considerable height as they can extend from the deep sea to thousands of meters above sea level. The topography of coastal volcanoes can be complex and asymmetric due to the descent of one or more of their flanks for thousands of meters into the sea. For example, the southeastern flank of Mount Etna in Italy extends from ~3,350 m above sea level (a.s.l.) to ~1,800 m below sea level (b.s.l.) (Urlaub et al., 2022) and the southern flank of Kīlauea in Hawai'i descends from ~1,200 m a.s.l. to ~5,000 m b.s.l. (Smith et al., 1999).

Writing – review & editing: Megan Campbell, Séverine Furst, Henriette Sudhaus, Morelia Urlaub

It is not uncommon for the submerged portion of a volcano to be overlooked, as onshore areas are much easier to observe and monitor than offshore areas. However, onshore areas of volcanic islands typically only account for a small percentage (<10%) of the total volume of the edifice (Klein et al., 2023). Given that the majority of the edifice is submerged and that typical monitoring only considers the "tip of the iceberg", failure to monitor submerged flanks could lead to an underestimation of the potential hazard.

Monitoring marine volcanoes is particularly important due to the hazards they pose to coastal communities. For example, a tsunami caused 437 fatalities in coastal areas of Indonesia, following the flank collapse of Anak Krakatau in 2018 (e.g., Syamsidik et al., 2020). Different monitoring strategies can be used to assess potential volcanic hazards and one of the most effective techniques is to analyze volcano deformation. Volcano deformation can be observed from geodetic data, acquired from tiltmeters, Global Navigation Satellite Systems (GNSS), or Interferometric Synthetic Aperture Radar (InSAR). Current time series analysis methods of GNSS and InSAR reach a millimeter resolution (Biggs & Wright, 2020; Hager et al., 1991) allowing multi-scale observations of deformation to be made. This data can then be used in analytical and numerical modeling methods to characterize different sources of deformation and to improve our understanding of magmatic and volcano-tectonic processes.

Analytical models provide a computationally efficient solution to volcano deformation problems due to solving closed sets of equations relating sources of deformation to ground deformation signals (Lisowski, 2007). These models are most commonly solved in homogeneous, elastic, half-space media, where a half-space source is embedded in a domain with a flat, free surface. Deformation sources that involve complex source shapes are algebraically difficult to solve (Nikkhoo, 2019), thus, only simple source shape solutions exist. For example, the point source approximation (Mogi, 1958), and, spherical and ellipsoidal magma chambers (Davis, 1986; McTigue, 1987) are commonly used to characterize magmatic sources in different volcanic settings. Despite their popularity for solving volcano deformation problems, limitations in their resultant approximations exist such that the Mogi (1958) and Davis (1986) solutions are only valid in approximating far-field displacements, and, the McTigue (1987) model validity is constrained by depth and dimensions of the source parameters (Nikkhoo, 2019; Segall, 2010).

A further limitation of half-space solutions is that they typically ignore the effect of topography and this has been established as one of the most influential factors in modeling methods (Cayol & Cornet, 1998; Hickey et al., 2024; Johnson et al., 2019; Ronchin et al., 2015; Williams & Wadge, 1998). For example, overestimation of source volume change can be up to 50% for volcanoes with slopes of 30° (Cayol & Cornet, 1998), leading to erroneous interpretations of deformation sources. These conclusions were made based on axisymmetric approximations which overlook natural variations in the topographic surface and complexities from submerged flanks. In order to better account for topography in half-space solutions, approximations for the effect of topography were developed. This allowed topography to be accounted for by varying the depth of the source at specific surface points (Williams & Wadge, 1998) or by making a first-order approximation to a zero-order characterization of the slope (Williams & Wadge, 2000). These approaches have commonly been used to account for the effect of topography in different modeling studies (e.g., Lungarini et al., 2005; Montgomery-Brown et al., 2009). Further work has assessed the importance of the effect of topography on deformation modeling by using numerical models to investigate how it interplays with varying material properties (e.g., Hickey et al., 2024), and other works have found that resultant displacement patterns can be correlated to topographic features, such as steep slope changes (e.g., Johnson et al., 2019; Ronchin et al., 2015). Furthermore, advanced models that incorporate viscoelasticity and varying rheologies find that topography plays a minor role in the resultant deformation pattern (Trasatti et al., 2003).

Whilst using an approximation for the effect of topography can be beneficial, approaches exist which include the complete topographic surface in a simple analytical model. Using a full space modeling domain allows a complete and variable free surface. Until recently, the only solutions solvable in a full space were angular and polygonal dislocations by Yoffe (1960), Brown (1975), and Comninou and Dundurs (1975), however, long-standing artifact problems existed making it challenging to use as a solution to volcano deformation problems (Nikkhoo, 2019). Nikkhoo and Walter (2015) adapted the triangular dislocation solution by Yoffe (1960) such that their solution became numerically stable and free of artifact singularities: allowing for complex source geometries to be solved for within a model space containing realistic topographic surfaces.

21699356, 2025, 8, Downloaded from https://agupubs.onlinelibrary.wiley.com/doi/10.1029/2024JB030805 by Karlsruher Institut für Technologie, Wiley Online Library on [02/09/2025]. See the Terms and Conditions (https://onlinelibrary.wiley.com/terms-and-conditions) on Wiley Online Library for rules of use; OA articles are governed by the applicable Creative Commons License

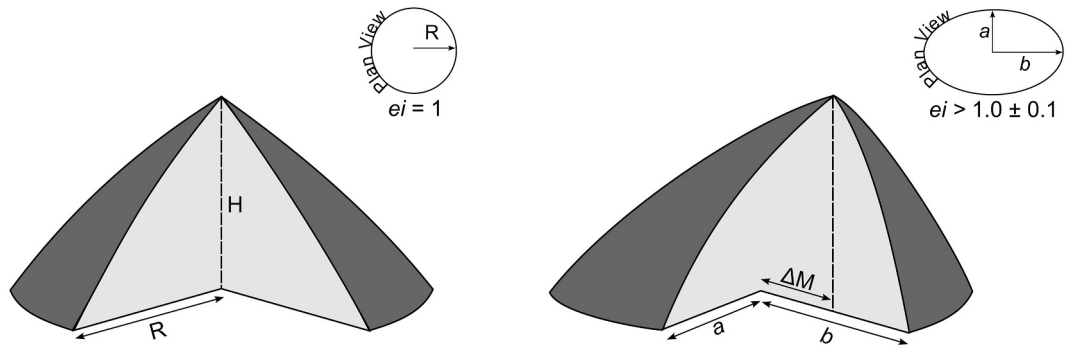

Figure 1. Axisymmetric (left) and asymmetric (right) depictions of a volcanic edifice. The axisymmetric cone is characterized by the height, H, the radius of equivalent edifice area, R and an $ei = 1$. The asymmetric volcano has a height, H, and a maximum and minimum radii of the basal circumference, b and a, respectively. The offset of the peak from the centroid is defined as ΔM.

The inclusion of topography and complex sources of deformation is now possible in analytical solutions for volcano deformation. With these new prospects, we aim to investigate how the natural range of topographic parameters may inform us of the importance of complete edifice topography (from the submarine base to the subaerial peak) in volcano deformation analyses. To do so, we apply a geomorphometric parameterization to improve the existing characterization of marine volcano shapes for deformation purposes. We implement the *Triangular Dislocation* solution by Nikkhoo and Walter (2015) making use of existing meshing methods to create discretized sources and the complete topographic surface. The relationship between the geomorphometric parameters and the resultant deformation field is evaluated by performing model simulations on synthetic cases and three case studies representing the full spectrum of the topographic parameters: Mount Etna and Stromboli in Italy, and El Hierro in the Canary Islands. Finally, we contextualize our results and discuss their implications for volcano deformation modeling and monitoring of marine volcanoes.

2. Methods

2.1. Geomorphometric Parameterization of Marine Volcanoes

Marine volcanoes hereby refer to partially submerged island and coastal volcanoes. To classify the shape of marine volcanoes, we extract parameters related to the shape, slope, and size of a volcanic edifice from a geomorphometric database by Klein et al. (2023), which contains information on 47 marine volcanoes. The parameters are obtained from a GIS-based model, which requires a Digital Elevation Model (DEM) of the volcano edifice and a delineation to mark the edifice boundary. The delineation is defined by a slope discontinuity of 3° (van Wees et al., 2024), which in some marine settings can be difficult to distinguish (Klein et al., 2023). For this reason, we only consider 17 of the marine volcanoes from the database, as these are independent volcanoes with clearly defined edifice boundaries and either a recent eruptive history, or a central eruptive area or crater.

We select three parameters from the database that effectively describe the topography of marine volcanoes (Figure 1). First, we consider the steepness parameter, H/R, where the total height, H, is the difference between the summit elevation and the elevation of the lowest point of the edifice boundary, and R, is the radius of a circle with an area equivalent to that of the total edifice (Klein et al., 2023). Second, we consider ΔM, a measure of offset between the centroid of the volcano and the topographic peak, which is a proxy for edifice asymmetry (Klein et al., 2023). This is given by the planar distance between the topographic peak and the centroid of the polygon enclosed by the edifice boundary, normalized by R to yield a dimensionless parameter between 0 and 1. When the centroid and summit are in the same location, $\Delta M = 0$, and when $\Delta M = 1$ the distance between points is equal to R (Klein et al., 2023). Lastly, we use ei, the ellipticity index, a dimensionless parameter defining the elongation of the edifice boundary. A circular base will yield $ei = 1.0$ and for elliptical bases $ei > 1.0 \pm 0.1$. This is calculated by dividing the area of a circle defined by the maximum semi-axis of the basal polygon, b (see Figure 1), by the area of the edifice, A: $ei = \frac{\pi b^2}{A}$. In order to describe the complex topography of a marine volcano effectively, we multiply ΔM and ei together as a proxy for asymmetry, ΔM_{ei}. This combination of axial offset and ellipticity gives a first-order approximation of the topographic shape of the edifice. Axisymmetric volcanoes yield

21699356, 2025, 8, Downloaded from https://agupubs.onlinelibrary.wiley.com/doi/10.1029/2024JB030805 by Karlsruher Institut für Technologie, Wiley Online Library on [02/09/2025]. See the Terms and Conditions (https://onlinelibrary.wiley.com/terms-and-conditions) on Wiley Online Library for rules of use; OA articles are governed by the applicable Creative Commons License

21699356, 2025, 8, Downloaded from https://agupubs.onlinelibrary.wiley.com/doi/10.1029/2024JB030805 by Karlsruher Institut für Technologie, Wiley Online Library on [02/09/2025]. See the Terms and Conditions (https://onlinelibrary.wiley.com/terms-and-conditions) on Wiley Online Library for rules of use; OA articles are governed by the applicable Creative Commons License

an $ei = 1$ and $\Delta M = 0$, thus $\Delta M_{ei} = 0$, due to their symmetric circular base, whereas ΔM_{ei} for asymmetric volcanoes increases with increasing asymmetry and elongation.

For the 17 volcanoes considered in this study, we extract their geomorphometric parameters for the entire volcanic edifice (entire-extent metrics) and use the model from Klein et al. (2023) to calculate onshore-only metrics for the same volcanoes as a comparison. Finally, as a comparison to previous studies, we create three axisymmetric volcanoes ($\Delta M_{ei} = 0$) with different slopes of 10°, 20°, and 30° (see Cayol & Cornet, 1998), equivalent to varying values of H/R.

2.2. Model Set-Up

To simulate surface displacements on a volcano, a deformation source at depth and a domain description are required. We assume a Poisson ratio of $\mu = 0.25$, in a homogeneous full space modeling domain for each simulation. For the source, we consider volume changes associated with the inflation of a spherical magmatic reservoir. To model the source deformation, we take advantage of the analytical solutions provided by Nikkhoo and Walter (2015) for the 3D surface displacement and stress induced by a tensile opening and slip on a triangular dislocation. The solution adapts the triangular dislocation solution by Yoffe (1960), implementing more computationally efficient equations for the Burgers functions, which are used to calculate the displacement associated with a dislocation. The Nikkhoo and Walter (2015) solution divides the uniform modeling space into two, solving two sets of closed equations to create a solution free from artifacts and numerical instabilities. We set the domain as an elastic full space, allowing for a topographic free surface to be specified. This solution is independent of scale and input parameters, such as size, location, and slip vectors, allowing for different geophysical settings to be modeled.

Although a magmatic reservoir cannot be approximated by a single triangular dislocation, it can be discretized into adjacent triangular elements. Discretization allows for the representation of a complex source shape, like a curved surface, without any discontinuities in the solution (Kuriyama & Mizuta, 1993; Maerten et al., 2005; Salzer et al., 2014). Spherical reservoirs are the most common magma chamber geometries assumed in modeling set ups (Crozier et al., 2023). *Distmesh* by Persson and Strang (2004) is used to create a discretized 3D spherical mesh of triangular elements. This requires an input radius and returns the node points as input for the model. An opening is then applied to each triangular element such that the sum is equivalent to an increase of the source radius, emulating magmatic inflation or an increase in chamber volume. This volume change forms the basis for calculating the opening exerted on each element in the discretized spherical sources. We assume the volume change, ΔV is equal to the difference between the volume after, V_a, and before, V_b, an impulse of magma to the chamber, that is, $\Delta V = V_a - V_b$. Using the equation for the volume of a sphere, $V = \frac{4}{3}\pi r^3$, we find the radius after an intrusion event and approximate the opening, o needed for the model simulations as the difference between the post-intrusion radius (r_a) and the pre-intrusion radius (r_b). This gives: $r_a = \sqrt[3]{\frac{3\Delta V}{4\pi} + r_b}$, where $o = r_a - r_b$.

The resultant deformation is calculated at the free surface calculation points, which are specified by input DEMs or synthetic surfaces. By utilizing a full space modeling domain, the free surface can be set at any elevation between $-\infty$ to $+\infty$. Therefore, the free surface is always defined from 0 m elevation or sea level, such that a topographic free surface will have values corresponding to the elevation and flat synthetic surfaces can be specified for different heights. We extract DEMs from Global Multi-Resolution Topography Data Synthesis (GMRT) (Ryan et al., 2009), which combines subaerial and submarine surfaces. GMRT collates global elevation data at 30 m resolution, the General Bathymetric Charts of the Ocean data set (GEBCO) at 15 arc-second (450 m) resolution, and when available, ship-based multibeam bathymetry at 100 m resolution. The DEM is converted to the surface calculation points by extrapolating a planar triangular mesh, generated by *Distmesh*. A triangular mesh is used because it better accounts for topographical changes and complexities that a quadrilateral grid might neglect. The planar mesh is large enough to cover three times the edifice DEM, ensuring that the edges are distant enough to avoid creating artifacts in modeling results (Mantiloni et al., 2023). The surface mesh in each modeling simulation contains 9,958 elements and is scaled to the desired size of each case study. The mesh element size increases exponentially from the center outward, where the finest elements are in the central third of the mesh.

Our implementation requires inputs for the source location, depth, and dimensions along with the dislocation openings. In each simulation, the Topography Model (TM) is compared to a No-Topography Model (NTM), which resemble the assumptions made in elastic-half space solutions with flat free surfaces, (see Davis, 1986;

21699356, 2025, 8, Downloaded from https://agupubs.onlinelibrary.wiley.com/doi/10.1029/2024JB030805 by Karlsruher Institut für Technologie, Wiley Online Library on [02/09/2025]. See the Terms and Conditions (https://onlinelibrary.wiley.com/terms-and-conditions) on Wiley Online Library for rules of use; OA articles are governed by the applicable Creative Commons License

McTigue, 1987; Mogi, 1958). An NTM is constructed by creating a flat free surface within the full space modeling domain following the same mesh generation steps outlined in this section (excluding the extrapolation step for the DEM). In previous studies, the flat surface is typically set at different elevations such as the peak, average elevation, or at sea-level with respect to the volcano considered. Following the recommendations of Cayol and Cornet (1998) and Williams and Wadge (1998), we compare two possible NTMs throughout this study: at the peak elevation (NTM-peak) and the average height of the volcano (NTM-AvH) for the parameter study and then only compare with NTM-peak for the case studies.

2.3. Testing the Relationship Between Asymmetry and Steepness

To test the relationship between the geomorphometric parameters, ΔM_{ei} and H/R, we create a model domain with a synthetic volcano topography, represented by a regular cone. The cone can be modified to apply different values of ΔM_{ei} and H/R. The height and ellipticity of the cone remain constant across all our simulations, where $H = 3{,}846.5$ m a.s.l., based on the average of the 17 volcanoes in our study, and $ei = 1$. By setting $ei = 1$, $\Delta M_{ei} = \Delta M$ for the parameter study. The spherical deformation source is made of 58 triangular elements. It is set to a depth of $d = 1$ km b.s.l., centered beneath the topographic peak, and has a source radius $a = 0.5$ km. The volume change of the source is equivalent to 3×10^6 m^3, with an opening, $o = 1$ m applied at each dislocation.

2.4. Case Study Applications

2.4.1. Real Topography and Identical Sources

To test the effect of geomorphometric parameters in topographic volcano deformation modeling, we apply the same deformation source to the three case studies using their real topography as the free surface calculation points. We chose three volcanoes that differ in setting and topographic relief: El Hierro, Stromboli, and Etna (Figure 2).

The same deformation source is applied to each setting, centered at 12 km b.s.l., beneath each volcano peak, with a radius of 0.5 km. The volume change was arbitrarily chosen and set to 7.8×10^6 m^3. Therefore, the source was made of 54 elements, and each had an opening of 2.5 m applied.

2.4.2. Real Topography and Realistic Sources

Using the three case studies introduced in Section 2.4.1, we derive source characteristics based on those described in literature to evaluate the effect of topography in each case study for an event of typical magnitude. Whilst the volume intruded into a magma chamber is not equivalent to the volume erupted due to the balance of magma compressibility and the material properties of the host rock (McCormack Kilbride et al., 2016), we use values from the literature for either the volume change of the chamber or the volume of the erupted material and approximate constraints on the typical order of magnitude of volume change at each case study. We assume that the literature-derived parameters are realistic and representative of a source at each volcano, in the past and possibly in the future.

2.5. Case Studies Setting and Source Context

2.5.1. El Hierro

El Hierro is situated on the southernmost edge of the Canarian archipelago, off the coast of western Africa. The island comprises three convergent rifts, separated by three landslide embayments: El Golfo (eG), El Julan (eJ) and las Playas (lP) which are visible both onshore and offshore (Figure 2a) (López et al., 2012). The island has grown from a depth of 3,793 m b.s.l and reaches a maximum elevation of 1,490 m a.s.l.. The island is over 5,284 m in total elevation, with only 2.3% of its volume above sea level.

The most recent and well-monitored eruption on El Hierro was submarine and occurred in October 2011 near the southernmost tip of the island (Carracedo et al., 2012; González et al., 2013). The eruption was well monitored, with seismicity, ground deformation and gas emissions recorded from onshore instrumentation (Martí et al., 2013). Seismicity records indicated the presence of an intermediate reservoir at a depth of 10–12 km b.s.l., responsible for the erupted magma (Martí et al., 2013). The volume of erupted material was estimated to be $\sim 2 \times 10^8$ m^3, which should match the volume intruded into the reservoir (Martí et al., 2013). Based on this study, the source radius was

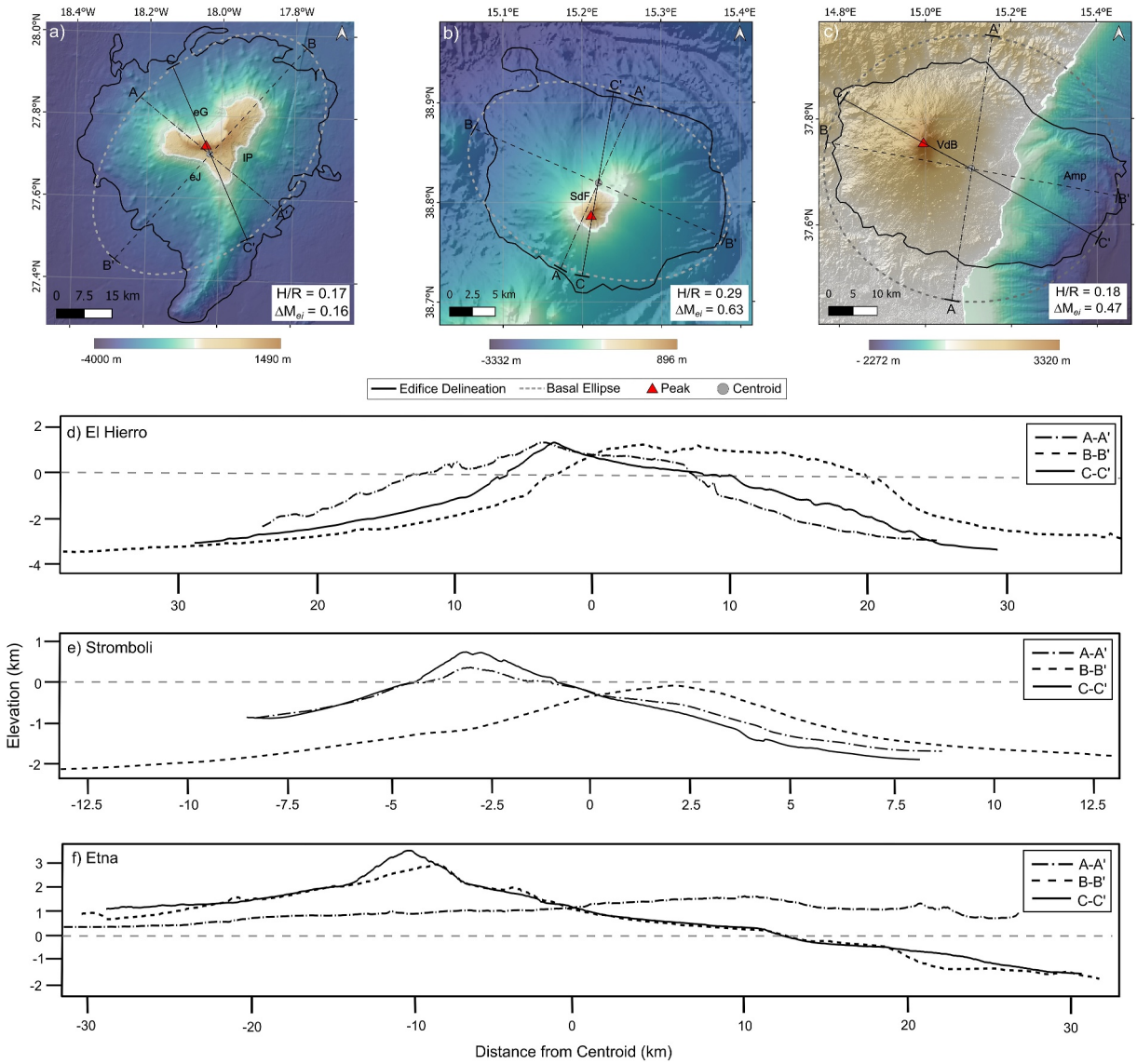

Figure 2. Case Study volcanoes: (a) El Hierro, (b) Stromboli and (c) Etna. Each panel shows the volcanic edifice delineation in black defined by the 3° contour line, and the gray line indicates the basal ellipse (Klein et al., 2023). The topographic peak is given by the red triangle in each plot and is coincident with the source location in models involving case studies. Each map shows geomorphologic features in the landscape: in El Hierro eG–El Gorgo, eJ–el Julan, lP–las Playas; Stromboli SdF–Sciara del Fuoco; and Etna VdB–Valle del Bove and Amp - Amphitheater. Using the ellipse, the black lines show the cross-section lines through the minor axis A–A′, major axis B–B′, and through the plane defined by ΔM_{ei} C–C′. The topographic profiles are shown in (d)–(f) for each volcano respectively. Note the differences in horizontal and vertical scales.

approximated by the spatial distribution of seismicity and assuming a spherical magma chamber, we set $a = 2.5$ km as the average area of the seismicity is 5 km in length. We set $d = 12$ km b.s.l. beneath the topographic peak at $X = 18.0°$W, $Y = 27.7°$N. The source consists of 54 elements and an opening of $o = 2.5$ m was exerted on each dislocation, equivalent to a volume change of 2×10^8 m^3.

2.5.2. Stromboli

Stromboli, a volcanic island in the Tyrrhenian Sea off the coast of southern Italy, is one of the world's most active volcanoes, renowned for its persistent Strombolian activity. A notable feature of the edifice is the steep landslide scar, the Sciara del Fuoco (SdF, Figure 2b), located on the northwest side of the island, which experiences well-documented deformation and slope instability (Casalbore et al., 2010; Di Traglia et al., 2021). Stromboli edifice

21699356, 2025, 8, Downloaded from https://agupubs.onlinelibrary.wiley.com/doi/10.1029/2024JB030805 by Karlsruher Institut für Technologie, Wiley Online Library on [02/09/2025]. See the Terms and Conditions (https://onlinelibrary.wiley.com/terms-and-conditions) on Wiley Online Library for rules of use; OA articles are governed by the applicable Creative Commons License

21699356, 2025, 8, Downloaded from https://agupubs.onlinelibrary.wiley.com/doi/10.1029/2024JB030805 by Karlsruher Institut für Technologie, Wiley Online Library on [02/09/2025]. See the Terms and Conditions (https://onlinelibrary.wiley.com/terms-and-conditions) on Wiley Online Library for rules of use; OA articles are governed by the applicable Creative Commons License

rises ~3,582 m from the seafloor, with only the top 924 m exposed above sea level. This area above sea level only accounts for 0.5% of the total volume of Stromboli.

Despite the extensive onshore monitoring of Stromboli island (Di Traglia et al., 2015), source modeling remains challenging due to its near-continuous eruptive activity. Some studies have suggested different magma storage zones within the edifice. For example, a shallow reservoir above sea level is well-documented through geophysical and geochemical studies. This is said to feed Strombolian activity and is postulated to be between to 600 m a.s.l. (Di Traglia et al., 2014). Di Traglia et al. (2015) analyses this reservoir by inverting InSAR data and find that 4.7×10^5 m^3 was the cumulative volume change over the period of Strombolian activity from 2010 to 2014. Additionally, an intermediate reservoir between 1,500 m b.s.l. and 2,000 m b.s.l. has also been postulated from seismic tomography (Patanè et al., 2017) and the inversion of geodetic data (Di Traglia et al., 2015). Given that Stromboli is an active open conduit basaltic volcano (Petrone et al., 2022; Viccaro et al., 2021), we chose to model inflation from a reservoir at d = 1,800 m b.s.l., an average depth following those suggested by Patanè et al. (2017) and Di Traglia et al. (2015). Without any further constraints regarding the volume change and lateral extent of the intermediate reservoir, we set a = 0.25 km as the intermediate reservoir covers an area with a diameter of 0.5 km and d = 1.8 km b.s.l. beneath the topographic peak of Stromboli at $X = 15.2$°E, $Y = 38.8$°N. We set $o = 0.6$ m, equivalent to a volume change of 4.7×10^5 m^3, from Di Traglia et al. (2015).

2.5.3. Etna

Located in eastern Sicily, southern Italy, Mount Etna stands as one of Europe's most active volcanoes. It is located within a complex tectonic setting shaped by the Eurasian-African collision zone (Azzaro et al., 2013). Its dynamic geological setting, influenced by both local and regional tectonic factors, contributes to the volcano's flank instability (Acocella et al., 2013; Bonaccorso et al., 2013). The edifice reaches a total height of ~5,150 m, measured from the seafloor at ~1,800 m b.s.l. up to its summit at 3,350 m a.s.l.

Unlike other volcanoes in this study, Etna is a coastal volcano, meaning that most of its edifice is onshore, with approximately one-third offshore. Etna is one of the world's most extensively monitored volcanoes, benefiting from a large and comprehensive geophysical network that enables near real-time monitoring of its deformation. Studies of ground deformation linked to eruptive phases of Mount Etna have often considered GPS, InSAR, and tiltmeter data sets (Bonaccorso, 2001; Currenti et al., 2008; Palano et al., 2008). Notably, Bruno et al. (2022) analyze four inflation phases recorded by these methods in the period leading up to the December 2018 eruption. Within their study, an inflation event occurred during phase three and was interpreted by a source located at ~5,500 m b.s.l., with a volume change of 3.8×10^6 m^3. Assuming a spherical magma chamber made of 54 elements, we set a = 0.5 km and $o = 1$ m, equivalent to a volume change of 3×10^6 m^3. The source had a depth of 5 km b.s.l. and was located below the topographic peak at $X = 15.0$°E, $Y = 37.8$°N.

3. Results

3.1. Topographic Parameter Evaluation

The geomorphometric parameter distribution of asymmetry and steepness is highly variable for marine volcanoes (Figure 3a). The distribution of real cases deviates from axisymmetric assumptions (A, B, and C in Figure 3a), highlighting the variable nature of volcano topography and the underestimation from axisymmetric approximations (see Figure S1 in Supporting Information S1). The entire-extent metrics vary between ΔM_{ei} values of 0.15–1.49, where a main metric cluster occurs between 0.15 and 0.61, and H/R ratios of 0.11–0.29 (Figure 3a). Onshore-only metrics cover a wider range of asymmetry and steepness values: with ΔM_{ei} ranging between 0.03 and 1.50, and H/R ratios between 0.07 and 0.47. The onshore-only metrics are more widely spread compared to entire-extent metrics. However, no consistent pattern emerges between the difference of the entire-extent and onshore-only metrics, highlighting the case-specific nature of each volcano's topography (Figure 3b). Therefore, geomorphometric parameterization and whole or partial edifice distinction are crucial to providing an accurate topographic description.

3.2. Assessment of Asymmetry and Steepness

Using the previously characterized parameter ranges from the cluster of entire-extent metrics, we simulate synthetic volcanoes as outlined in Section 2.3 to evaluate the impact of asymmetry and steepness on surface

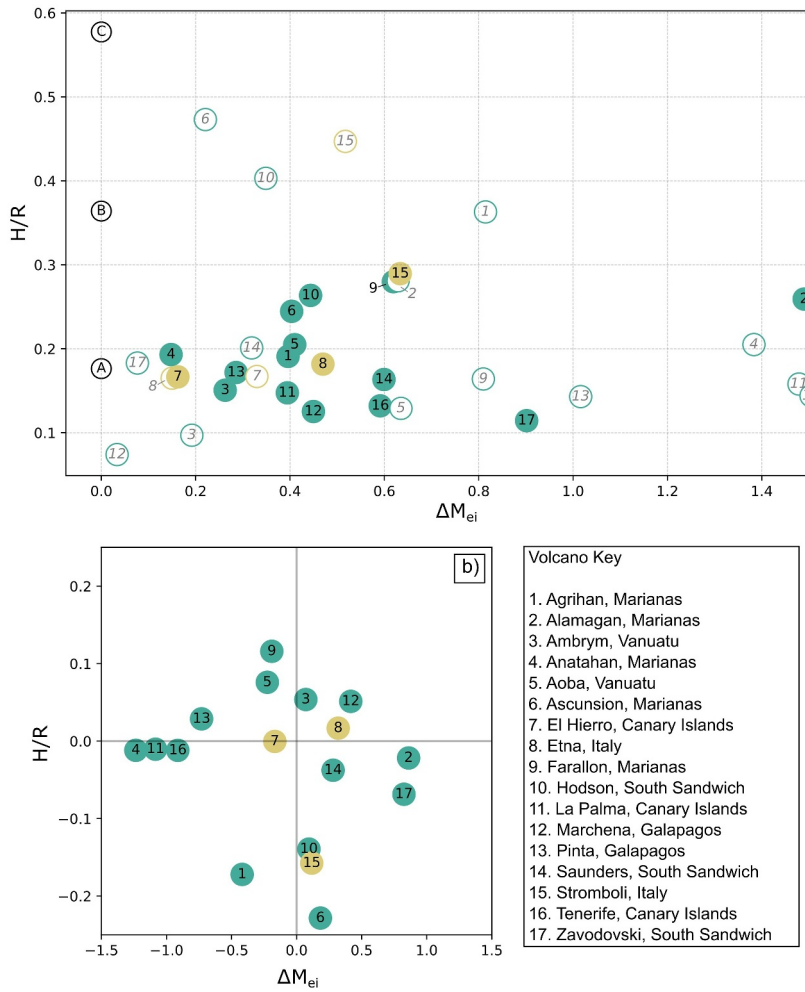

Figure 3. (a) Distribution of ΔM_{ei} and H/R ratio of the volcanoes considered in this study. Each symbol is numbered and corresponds to a specific volcano. Colored symbols represent metrics for the entire edifice, and hollow symbols represent onshore-only. Black hollow symbols (A, B, and C) represent axisymmetric comparison from Cayol and Cornet (1998) of volcanoes with slopes of 10°, 20° and 30°. (b) Difference between two groups of metrics (entire-extent minus onshore-only). The key lists the volcanoes considered from the Klein et al. (2023) database.

deformation. Based on our reference axisymmetric case (RAC), where $\Delta M = 0.0$ (Figures 4a and 4b), we observe that the maximum magnitude of displacement increases with increasing H/R. In addition, as the H/R ratio increases, a single peak in vertical displacement, U_z, gives way to the development of two maxima, separated by a local minimum. The two maxima increase as the H/R ratio rises (Figure 4a). Similarly, the peak in the horizontal displacement component, U_h, moves further away from the center with increasing H/R (Figure 4b). Without introducing asymmetry, increasing steepness results in more than a tenfold increase in U_z and approximately a sevenfold increase in U_h. Furthermore, the TM cases deviate away from the NTMs, where the NTM-peak solution is more comparable to the case results with topography, therefore we discuss results in reference to this NTM.

By introducing asymmetry ($\Delta M = 0.1$, Figures 4c and 4d), we notice a slight increase in the maximum component of displacement compared with the RAC. However, we note that there is a greater increase for cases with larger H/R, for example, where $H/R = 0.1$ both components increase by <0.1 mm, whereas for $H/R = 0.5$, U_z has increased by 2.0 mm and U_h by 4.7 mm, when compared with the RAC. The increase in maximum displacement with increasing asymmetry and steepness is apparent for all model results (Figures 4e–4n), where the steepest cones experience a greater signal of deformation. In both components of displacement, the rate of maximum amplitude increase is exponential, such that the greater the asymmetry and steepness of the cone, the greater the change from the NTM would be (Figure S2 in Supporting Information S1). The effect is more pronounced for the

21699356, 2025, 8, Downloaded from https://agupubs.onlinelibrary.wiley.com/doi/10.1029/2024JB030805 by Karlsruher Institut für Technologie, Wiley Online Library on [02/09/2025]. See the Terms and Conditions (https://onlinelibrary.wiley.com/terms-and-conditions) on Wiley Online Library for rules of use; OA articles are governed by the applicable Creative Commons License

21699356, 2025, 8, Downloaded from https://agupubs.onlinelibrary.wiley.com/doi/10.1029/2024JB030805 by Karlsruher Institut für Technologie, Wiley Online Library on [02/09/2025]. See the Terms and Conditions (https://onlinelibrary.wiley.com/terms-and-conditions) on Wiley Online Library for rules of use; OA articles are governed by the applicable Creative Commons License

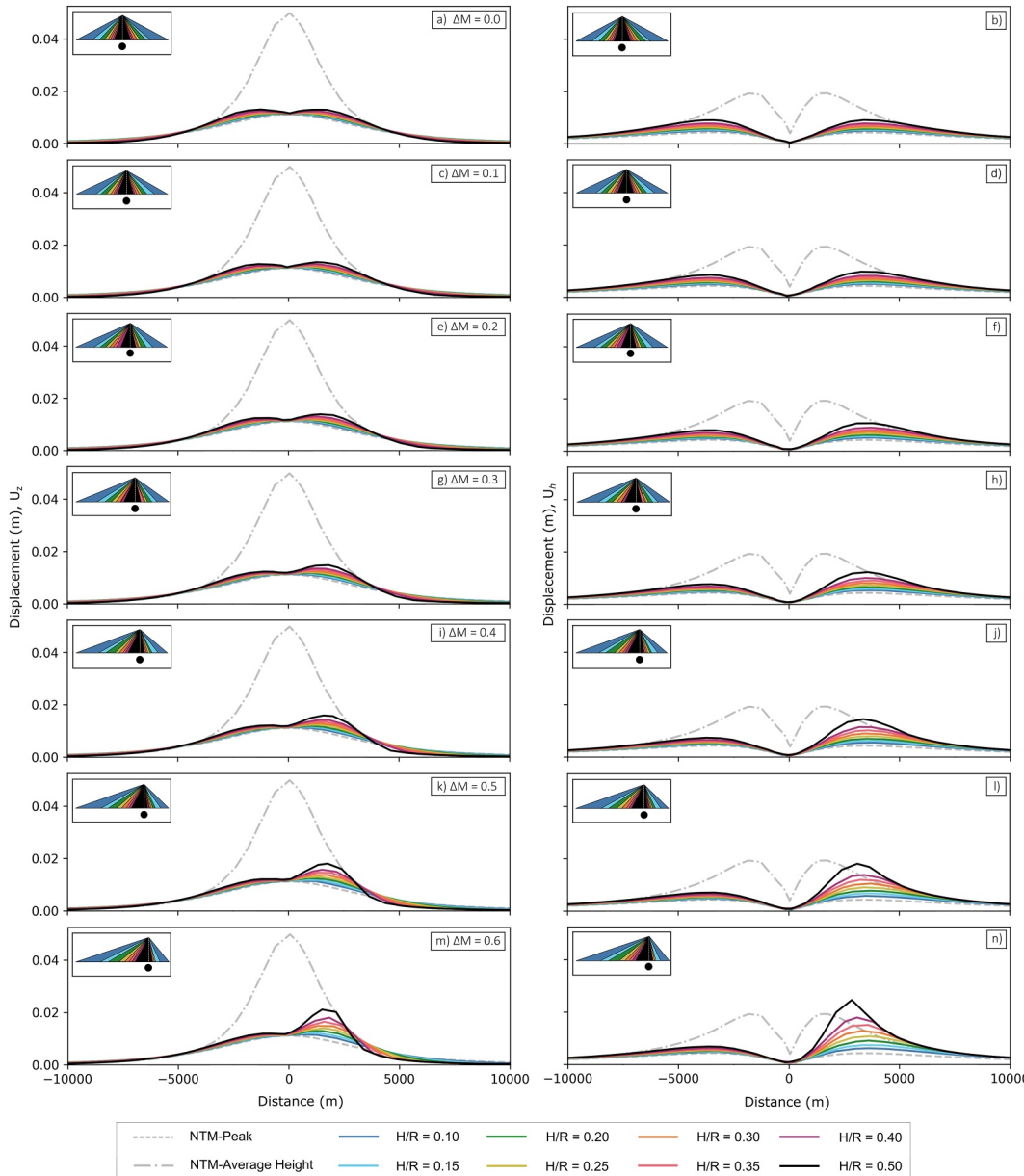

Figure 4. Vertical (first column) and horizontal (second column) displacements through the plane of offset (ΔM) of the cone. Each row corresponds to a value of ΔM_{ei}: (a–b) = 0.0, (c–d) = 0.1, (e–f) = 0.2, (g–h) = 0.3, (i–j) = 0.4, (k–l) = 0.5, and, (m–n) = 0.6. Each colored line in the crossed sections corresponds to the H/R ratio of the synthetic cone tested from 0.1 to 0.5. The dashed and dashed-dotted lines correspond to comparable no-topography models, where the flat elevation is calculated for NTM-peak and NTM-AvH, respectively. A schematic of the synthetic cone is shown in each panel's upper left corner.

horizontal component, where the steepest flank experiences greater than 1 mm increase (close to the resolution limit of GNSS and InSAR analyses techniques) for cones of $H/R > 0.15$ and all ΔM. For cones with $H/R > 0.30$ and all ΔM, the difference between the TM and NTM-peak is greater than 1 mm for all geomorphometric parameter pairs. For the cones with lower H/R, for example, $H/R = 0.15$ and $H/R = 0.20$, the effect is greater than 1 mm for $\Delta M > 0.6$ and 0.4 respectively. For the case with the largest asymmetry ($\Delta M = 0.6$, Figures 4m and 4n), the deviation of the NTM with the RAC is most pronounced, especially for the largest H/R. Overall, the horizontal component is more strongly influenced by the increasing complexity of the cone, with both its spatial distribution and magnitude affected more than those of the vertical component. There is also a

21699356, 2025, 8, Downloaded from https://agupubs.onlinelibrary.wiley.com/doi/10.1029/2024JB030805 by Karlsruher Institut für Technologie, Wiley Online Library on [02/09/2025]. See the Terms and Conditions (https://onlinelibrary.wiley.com/terms-and-conditions) on Wiley Online Library for rules of use; OA articles are governed by the applicable Creative Commons License

significant effect on the vertical component for cones with low steepness and high asymmetry, however more apparent for the cases of $H/R > 0.30$.

3.3. Influence of Realistic Topography

El Hierro, Stromboli, and Mount Etna represent a broad spectrum of the marine volcano geomorphometric parameters presented in Figure 3. El Hierro has a low edifice asymmetry ($\Delta M_{ei} = 0.16$) and low-average steepness ($H/R = 0.17$). Stromboli has high edifice asymmetry ($\Delta M_{ei} = 0.63$) and has the highest steepness ($H/R = 0.29$) in our database. Etna has high edifice asymmetry ($\Delta M_{ei} = 0.47$) and an average steepness ($H/R = 0.18$). In the following section, we describe the vertical and horizontal displacements for the TM, the NTM-peak, and the difference between modeled displacement, D, such that:

$$D = \mathrm{TM} - \mathrm{NTM}_{peak} \quad (1)$$

for modeled displacements from the same source of deformation.

The modeled displacement field varies in each case and reflects the topographic surface, clearly highlighting how different topographies above the same source of deformation, in Figures 5a, 5d, and 5g, influence both the magnitude and spatial distribution of the resultant deformation pattern. For example, the largest signal is concentrated within the landslide embayments (eG and eJ) on El Hierro, around the steep coastal and submarine areas to the southwest of Stromboli, and within the steep summit craters and into the VdB at Etna. These are all areas with slopes of >20° (Figure S3 in Supporting Information S1). The differences between TM and NTM in Figures 5c, 5f, and 5i, highlight that in distal regions the TM can overestimate the vertical component in comparison to the NTM. However, the magnitude of this difference is very small in comparison to the magnitude of displacement can be neglected. The horizontal displacements produced by the TM in Figures 6a, 6d, and 6g, also show differences in the magnitude and spatial distribution from the NTM in Figures 6b, 6e, and 6h. This topography-influenced pattern is prevalent on slopes further downslope from the maximum displacements observed for the vertical components. This is expected, as the horizontal component affects areas further downslope from the source, as found in the result from Section 3.2. The maximum horizontal displacement is confined to slopes with less steep slopes of <20° and in the base of the eG and eJ embayments, shallower slopes of the submarine flanks of Stromboli, and the VdB on Etna. The maximum magnitude of displacement is largest for Stromboli, which has the largest asymmetry and steepness values, and lowest for Mount Etna.

3.4. Influence of Realistic Sources

In Figure 7 we show the TM component displacements for each case study, considering a literature-derived source. The NTM and the corresponding differences are given in Figure S4 in Supporting Information S1 as they are scaled versions of the results shown in Figures 5 and 6. Each case study exhibits highly variable and distinct resultant displacement patterns, with variations reflecting the topographic surface of each volcano. The source at El Hierro is 5 times larger and 2.4 times deeper than the model in Section 3.3, thus the displacement pattern in this model simulation has a much larger magnitude and occurs over a larger area. The displacement pattern follows similar trends to those discussed in Section 3.3, such that the maximum displacement is concentrated within steep slopes for the vertical component and downslope of these areas for the horizontal component. The NTM for El Hierro underestimates the TM by 12% and 37%, for U_z and U_h, respectively, which are in detectable ranges for onshore geodetic monitoring equipment. The source at Stromboli is 2 times smaller and 2.7 times shallower than the model in Section 3.3, thus the displacement pattern is over a smaller area and has a smaller magnitude. The maximum components of displacement clearly follow similar trends to those previously described for the respective components. U_z is strongest in the southwest of the island, while the maximum horizontal displacement is mainly confined to the shallower slopes downslope from the region of the maximum vertical component, entirely offshore in this case. The TM is underestimated by 18% and 57% respectively for U_z and U_h. The source at Etna is the same as in Section 3.3, however, the opening is 2.5 times smaller. The TM model is underestimated by 10% and 37% respectively for the vertical and horizontal components of displacement.

In each case study, the onset of steep slopes coincides with an increase in the magnitude of displacement, which then decays with increasing distance from the projected source location on the surface. Areas that are proximally close to the sources but have shallower slopes, such as the ridge plateau on El Hierro, the northwest coast of

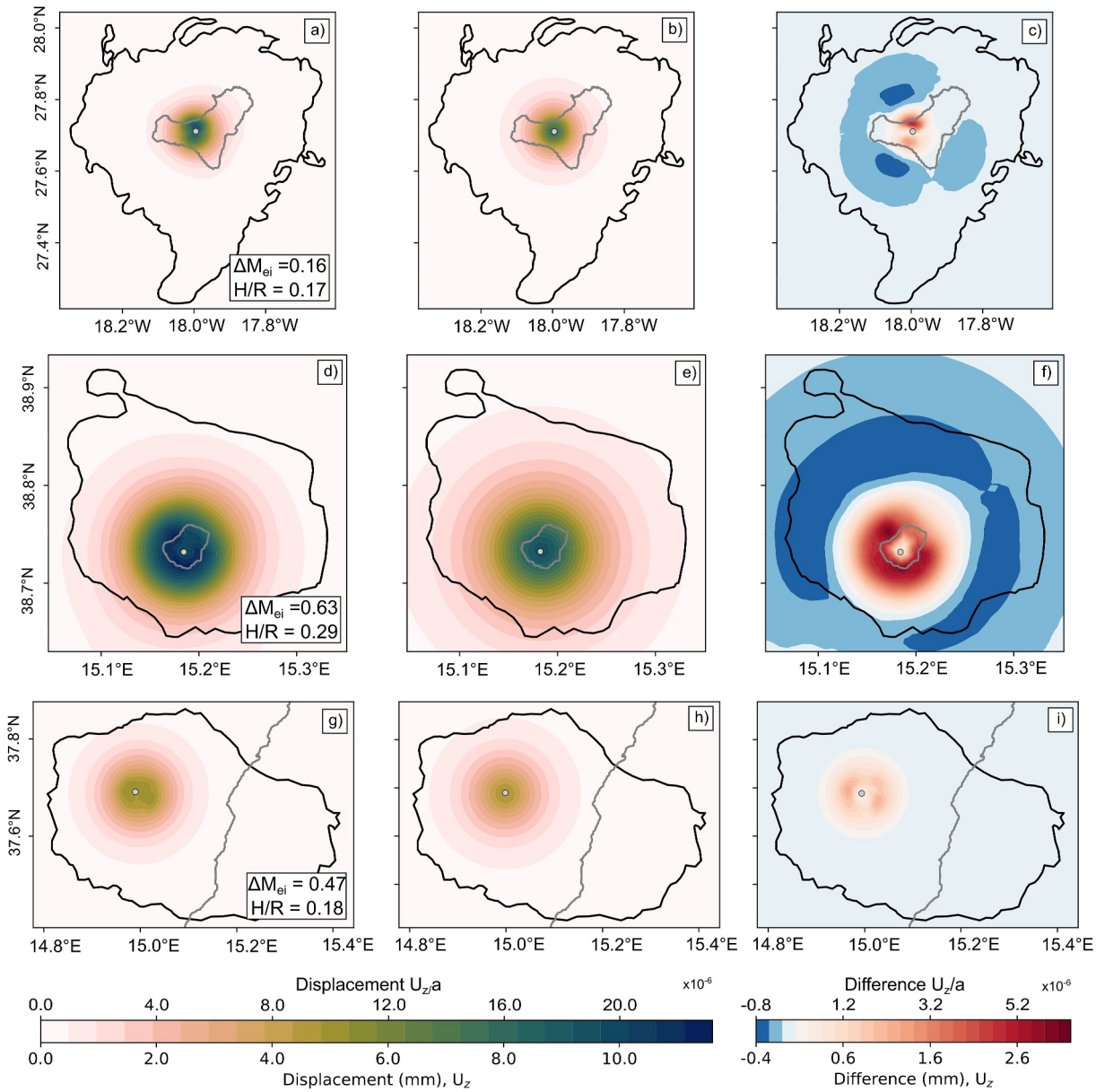

Figure 5. Vertical displacements induced by the inflation of a spherical source beneath each case study: El Hierro (first row, a–c), Stromboli (second row, d–f) and Etna (third row, g–i). The figure shows the results for the simulation with topography (first column: a, d, g), without topography (second column: b, e, h) and the difference between the two models without (third column: c, f, i). The source of deformation is constant and applied to the same depth b.s.l. to highlight the influence of topography at each case. The black line is the edifice delineation and the gray line is the coastline. The gray circle represents the source location.

Stromboli, and the southern flank of Mount Etna, have lower magnitudes of displacement compared to the areas with larger slope values. For the case of El Hierro and Stromboli, the largest signal is not limited to the subaerial area of the island, and can occur almost entirely offshore (horizontal component at Stromboli). Furthermore, at El Hierro and Stromboli the deformation signal can be over the entire edifice (up to the edifice boundary), which occur in deep water and are largely unmonitored.

4. Discussion

4.1. Geomorphometric Parameter Influence on Deformation Fields at Marine Volcanoes

We show that marine volcanoes have variable and distinct topographies that can be characterized by geomorphometric parameters. In particular, all volcanoes evaluated in this study are asymmetric, irrespective of the

21699356, 2025, 8, Downloaded from https://agupubs.onlinelibrary.wiley.com/doi/10.1029/2024JB030805 by Karlsruher Institut für Technologie, Wiley Online Library on [02/09/2025]. See the Terms and Conditions (https://onlinelibrary.wiley.com/terms-and-conditions) on Wiley Online Library for rules of use; OA articles are governed by the applicable Creative Commons License

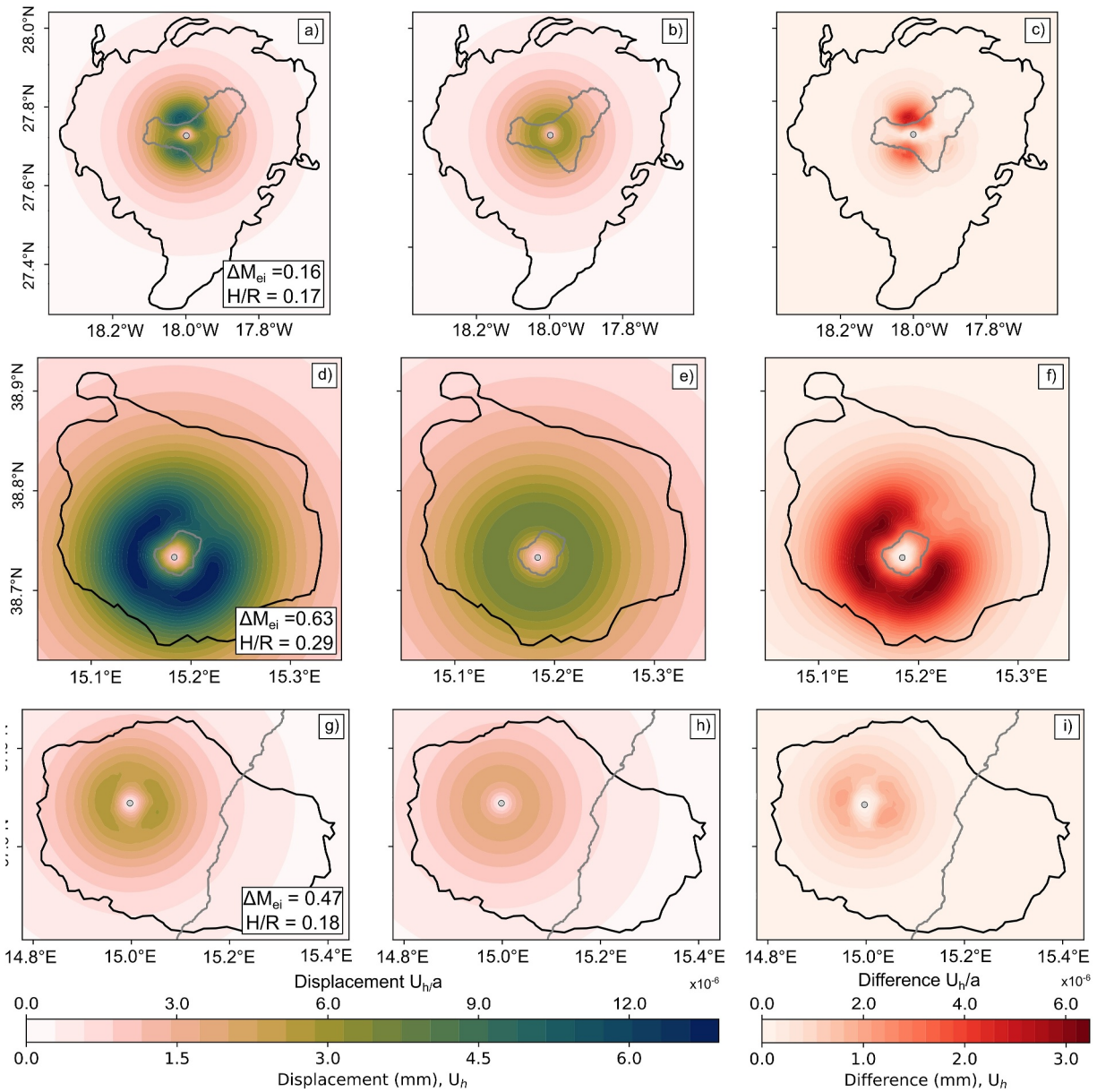

Figure 6. Horizontal displacements induced by the inflation of a spherical source beneath each case study: El Hierro (first row, a–c), Stromboli (second row, d–f) and Etna (third row, g–i). The figure shows the results for the simulation with topography (first columns: a, d, g), without topography (second column: b, e, h) and the difference between the two models without (third column: c, f, i). The source of deformation is constant and applied to the same depth b.s.l. to highlight the influence of topography at each case. The black line is the edifice delineation and the gray line is the coastline. The gray circle represents the source location.

extent to which they are being considered (onshore-only or entire-extent). The geomorphometric parameter values vary depending on which part of the edifice is considered and they differ in an irregular way (Figure 3b). For example, the onshore-only metrics for Stromboli are steeper ($H/R^{OnshoreOnly} = 0.45$) and less asymmetric ($\Delta M_{ei}^{OnshoreOnly} = 0.52$) compared with the entire-extent metrics whereas the onshore-only metrics for El Hierro have the same steepness ($H/R^{OnshoreOnly} = 0.17$) but more asymmetry ($\Delta M_{ei}^{OnshoreOnly} = 0.33$) than its entire-extent values. Etna has smaller geomorphometric parameter values when considering the onshore-only metrics, where $\Delta M_{ei}^{OnshoreOnly} = 0.15$ and $H/R^{OnshoreOnly} = 0.17$. Therefore, when describing volcano shape it is crucial to define which part of the edifice is being considered as parameter values can change significantly between areas of definition.

21699356, 2025, 8, Downloaded from https://agupubs.onlinelibrary.wiley.com/doi/10.1029/2024JB030805 by Karlsruher Institut für Technologie, Wiley Online Library on [02/09/2025]. See the Terms and Conditions (https://onlinelibrary.wiley.com/terms-and-conditions) on Wiley Online Library for rules of use; OA articles are governed by the applicable Creative Commons License

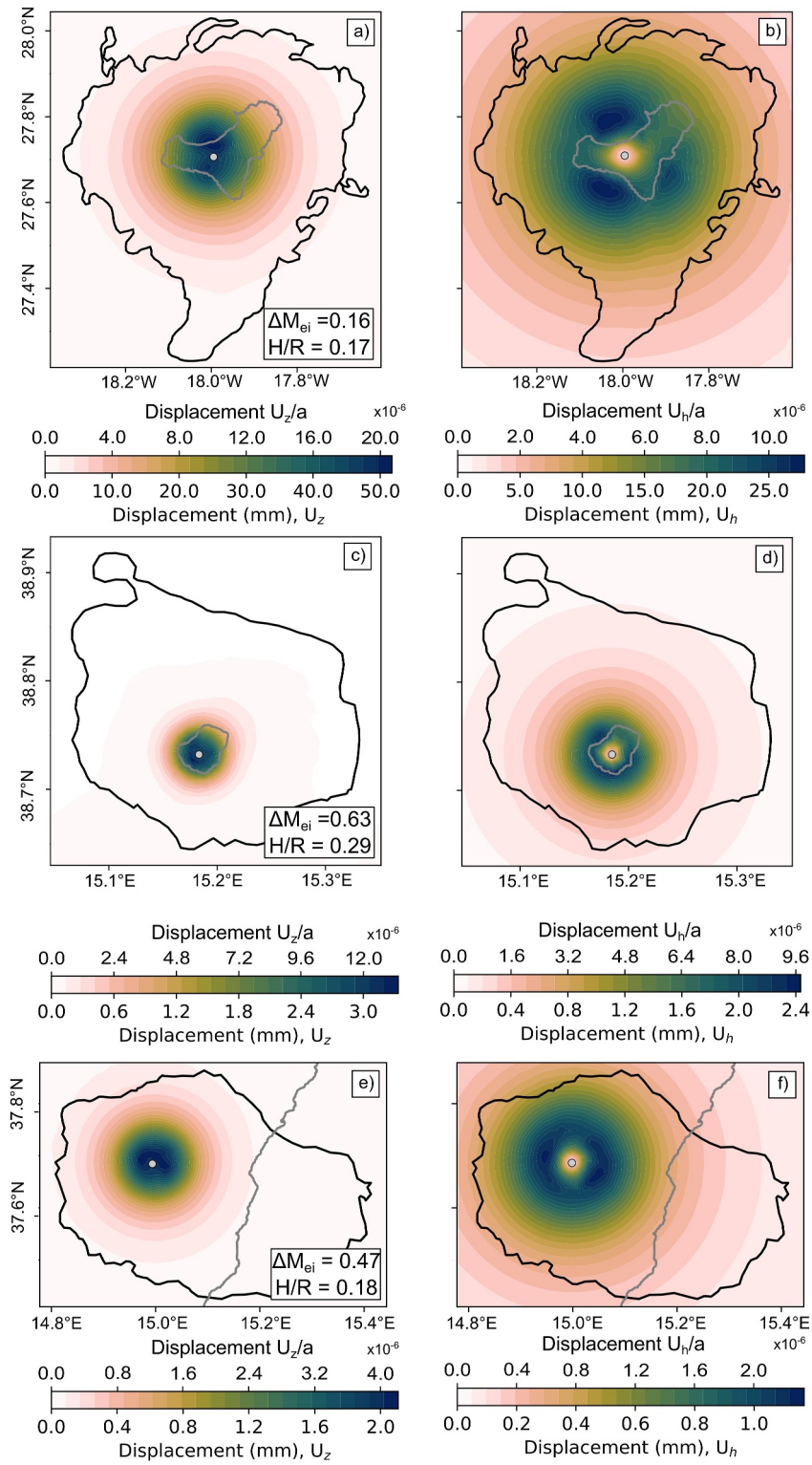

Figure 7. The vertical (first column: a, c, e) and horizontal (second column: b, d, f) displacements are simulated at each case study for a literature-derived source of deformation: El Hierro (first row: a, b), Stromboli (second row: c, d) and Etna (third row: e, f). The black line is the edifice delineation, and the gray line is the coastline. The gray circle represents the source location.

21699356, 2025, 8, Downloaded from https://agupubs.onlinelibrary.wiley.com/doi/10.1029/2024JB030805 by Karlsruher Institut für Technologie, Wiley Online Library on [02/09/2025]. See the Terms and Conditions (https://onlinelibrary.wiley.com/terms-and-conditions) on Wiley Online Library for rules of use; OA articles are governed by the applicable Creative Commons License

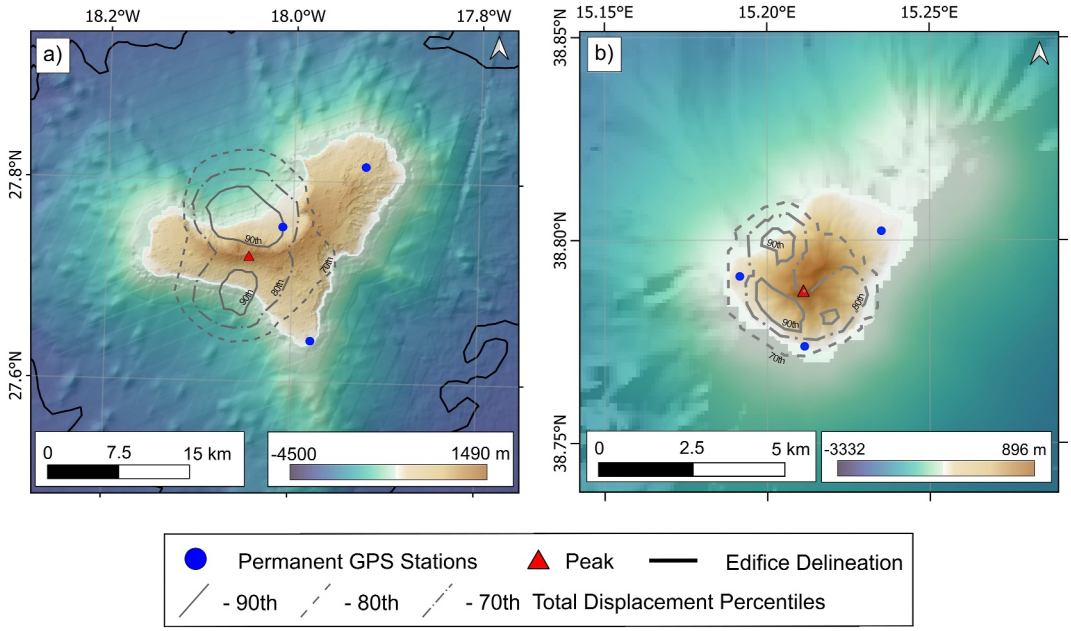

Figure 8. 70th, 80th, and 90th Total Displacement Percentiles for El Hierro (a) and Stromboli (b). The blue circles represent the permanent GNSS stations on each island.

The results of the parameter study indicate that as steepness and asymmetry increase, the deviation of a model considering true topography (TM) from a model with a flat surface (NTM) increases. This deviation is higher than the resolution limit of current GNSS and InSAR analyses techniques for almost all parameter pairs, especially for the horizontal component. The increase in deviation is explained via positive exponential trends (Figure S2 in Supporting Information S1), such that the geomorphometric parameter pairs with the largest values would have the largest deviation from an NTM.

Providing the relationship from the parameter study would hold for real cases, we expect the largest deviation from NTM-peak to occur at Stromboli, due to the large ΔM_{ei} and H/R, and the opposite to be true for El Hierro which has the lowest geomorphometric parameter values. In the case study with the same source, we see that Etna has the smallest magnitude of displacement. However, this discrepancy can be explained due to the setting of Etna on the coast. The cross sections in Figure 2f illustrate that Etna has an uneven distribution of topography, such that ~66% of the edifice is onshore. The proximal area impacted by the deformation source is onshore (Figure 7), therefore we conclude that Etna is better described by the onshore-only metrics, since the submerged flank deformation is negligible. This means that Etna has the lowest geomorphometric parameter values in the case studies considered. This explains the lower magnitude of deviation from the NTM in comparison with the other cases. Despite the low geomorphometric parameter values, Etna still experiences a significant deviation of 10% for the vertical component and 37% for the horizontal component between the TM and the reference NTM. This highlights that even with low geomorphometric parameter values, the role of topography is significant and should be considered in deformation modeling.

The parameter study showed only small deviations between TM and NTM for low geomorphometric parameter values, however this was with a smooth surface representing the volcanic edifice. Therefore, it is clear from the model simulations with topography, that small-scale variations control the spatial and magnitude distribution of resultant displacement fields as we see the displacement pattern changes due to the influence of topographic features within the different edifices (Figures 5–7). Comparing the results from the parametric study to our case study results, we observe no correlation between the axis of ΔM and the location of the maximum displacement. This is because the smooth surface approximation in the parametric study (Section 3.2) underestimates the influence from the entire topographic surface. Therefore, there is no link between ΔM_{ei} and the spatial distribution of displacement as this is entirely dependent on the small-scale variations of the surface. With this, our results indicate that a first-order approximation of displacement magnitude deviation from NTMs can be made based on geomorphometric parameter values.

21699356, 2025, 8, Downloaded from https://agupubs.onlinelibrary.wiley.com/doi/10.1029/2024JB030805 by Karlsruher Institut für Technologie, Wiley Online Library on [02/09/2025]. See the Terms and Conditions (https://onlinelibrary.wiley.com/terms-and-conditions) on Wiley Online Library for rules of use; OA articles are governed by the applicable Creative Commons License

21699356, 2025, 8, Downloaded from https://agupubs.onlinelibrary.wiley.com/doi/10.1029/2024JB030805 by Karlsruher Institut für Technologie, Wiley Online Library on [02/09/2025]. See the Terms and Conditions (https://onlinelibrary.wiley.com/terms-and-conditions) on Wiley Online Library for rules of use; OA articles are governed by the applicable Creative Commons License

Previous studies have identified other aspects that could explain topographic importance. For example, Ronchin et al. (2015) explained that slope angle has a secondary effect on the expected displacement pattern, such that abrupt changes in topography cause an amplification effect leading to larger values of displacement, evident for both components. This is known as exposure (Ronchin et al., 2015). This is particularly true for steep sloped areas (Ronchin et al., 2015), which in this study would correspond to eG, eJ, SdF, and VdB landslide embayments in each respective case study (Figure 2). For the maximum vertical displacement in each case study, we find amplifications of the displacement magnitude, as these are found near the walls of the landslide embayments, and where the slope is steepest. However, the maximum horizontal displacement is less explained by exposure as this is not found on steep slopes but rather downslope in the shallower plateaus (at the base of these embayment areas in Figure 6).

Therefore, using the complete topography in deformation modeling is necessary as the resultant deformation pattern is case dependent and changes over topographic variations. This is not necessarily confined to steep slopes or high-gradient change areas, that is, for the horizontal component of displacement. Whilst defining topographic parameters can aid in descriptions of the shape of the volcano, they cannot be used as a method to predict where maximum displacements may occur. However, they can serve as a first-order indication of how much a volcano deformation scenario will be underestimated by a solution neglecting topography.

4.2. Implications for Monitoring Island Volcanoes

Our results indicate that incorporating the complete topography, of both subaerial and submarine flanks, of oceanic island volcanoes can yield important insights into where deformation will occur. Particularly at the two islands, El Hierro and Stromboli (Section 3.4), where by modeling a literature derived source, we observe that areas of highest deformation are located at the coast or entirely offshore (Figure 7). This highlights that traditional onshore monitoring may overlook areas of deformation from a realistic source of deformation. El Hierro and Stromboli have three permanent GNSS stations on them. Whilst spatially dense coverage can be obtained by InSAR observations, island volcanoes have specific limitations to InSAR coverage due to possibilities with land surface coherence (from fresh volcanic products, and/or vegetation), coastline signal loss due to radar absorption in water, temporal decorrelation (Simons & Rosen, 2015), and that their shape is unfavorable to satellite direction and coverage, for example, at Stromboli. Therefore, the need to improve land-based station coverage is evident in some volcanic island cases.

The sources modeled in Section 3.4, which represent realistic eruptive events, show that the areas of maximum displacement do not always coincide with the locations of the permanent GNSS stations on the island volcanoes studied (Figure 8). GNSS station placement is influenced by various logistical factors, including cost and accessibility, which often limit coverage. However, for volcanoes with recurrent eruptive episodes or well-constrained deformation sources, GNSS station placement could be optimized by considering the areas of greatest deformation in advance. For instance, a careful evaluation of expected displacements, alongside logistical constraints, can facilitate more strategic station placement to better monitor future deformation signals. In general, positioning instruments near coastal regions, which are more prone to deformation, would enhance signal detection. Additionally, if resources permit, deploying offshore instruments could further improve the spatial coverage of deformation at island volcanoes.

Prospects for monitoring offshore deformation are becoming more plausible. For example, offshore deformation is recorded at Axial Seamount in the Pacific Ocean, offshore Oregon, USA, where bottom-pressure instruments monitor vertical deformation (Chadwick et al., 2006, 2022). Similarly, during a recent seismic crisis offshore Santorini, bottom-pressure instruments recorded deformation associated with the dyke intrusion responsible for the seismicity (Isken and Karstens et al., 2025). Another case is at Mount Etna where acoustic baseline instruments have recorded fault slip offshore on the submerged southeast flank, approximately 10 km from the coastline (Urlaub et al., 2018). This particular experiment targeted gravitational motion, however, the technique measures changes in baselines which would be capable of detecting displacement signals associated with magmatic sources of deformation. By knowing where deformation signals will occur, regardless of the geodetic instrument, networks can be strategically designed if the source characteristics can be determined from previous unrest, and our modeling approach can be applied.

21699356, 2025, 8, Downloaded from https://agupubs.onlinelibrary.wiley.com/doi/10.1029/2024JB030805 by Karlsruher Institut für Technologie, Wiley Online Library on [02/09/2025]. See the Terms and Conditions (https://onlinelibrary.wiley.com/terms-and-conditions) on Wiley Online Library for rules of use; OA articles are governed by the applicable Creative Commons License

4.3. Evaluation of Model and Implementation

We make use of updated modeling codes and show that incorporating topography and discretized source shapes into an analytical solution for volcano deformation is achievable. Typical analytical solutions for volcano deformation include solutions for basic cavities in the subsurface (e.g., Davis, 1986; Fialko et al., 2001; McTigue, 1987; Yang et al., 1988). These are often regarded as simplified representations, which may not fully capture the complexity of volcanic subsurface settings, potentially leading to less accurate estimates of source volume or pressure changes when used in inverse modeling. Additionally, neglecting or approximating the topographic surface is a common approach in the application of analytical methods, largely due to the widespread availability and ease of use of existing codes (Battaglia et al., 2013; Crozier et al., 2023). To improve the representation of volcanic settings, finite element modeling can be used, which allows additional geophysical information such as heterogeneous material properties, irregular source geometries (from complex mesh patches), and the complete topographic surface to be included (e.g., Hickey & Gottsmann, 2014). These models can be laborious to implement, requiring user knowledge of specific software requirements, software licenses, and sufficient case study knowledge of material and medium properties to construct a representative model. These methods can have high computational costs, and even with additional information such as the material properties, oversimplified model results can arise from elastic considerations (Head et al., 2019). For example, viscoelastic modeling allows for a better consideration of the geothermal gradient present in volcanic systems (Del Negro et al., 2009; Newman et al., 2001), as magmatic intrusions and migration are long time-scale processes (Trasatti et al., 2003). In volcanic settings, the surrounding rocks are often heated beyond the brittle-ductile transition and do not behave in a purely elastic manner (Del Negro et al., 2009). Therefore, limitations persist with analytical and finite element solutions.

Despite the limitations of analytical solutions, they remain popular for tackling volcano deformation problems as they provide a timely first estimate of model parameters, which is useful for hazard and risk mitigation. Furthermore, due to code availability, usability, and improvements, they remain a popular method for a first analysis of deformation data (e.g., Battaglia et al., 2013). Therefore, having access to analytical solutions that incorporate complete topography and potential complex sources for timely analysis is a valuable asset. Our implementation of the Nikkhoo and Walter (2015) scripts enables a robust analysis for any volcano where a topographic DEM is available.

Our solution relies on the availability of open-source DEMs, which can be obtained from GMRT or other equivalent sources. Klein et al. (2023) compare high-resolution bathymetry with the GEBCO database in their geomorphometric analysis of marine volcanoes and emphasize the potential for slope characteristics to be underestimated by up to 15% when using low-resolution bathymetry. Therefore, low-resolution DEMs can still be used to analyze marine volcano deformation simulations, with the understanding that they may lead to an underestimation of topographical parameters.

5. Conclusion

We have investigated the role of topography in volcano deformation modeling at marine volcanoes. We have used an adapted, efficient analytical solution that includes topography and a discretized spherical source. By using geomorphometric parameters for classification, a comprehensive description of the complex topography of each volcano was achieved. This showed that as both asymmetry and steepness increase, the magnitude of maximum displacement also increases, implying that more complex topography exerts a greater influence on resultant displacement fields. This is observed in each case study, El Hierro, Stromboli, and Etna, where the largest deviation from a No-Topography Model (NTM) was observed at Stromboli, which had the largest steepness and edifice asymmetry parameter values. We showed that geomorphometric parameters can indicate how much a NTM will underestimate a TM however, the spatial distribution of the displacement is less explained by this technique and rather influenced by the individual variations of the topographic surface. In each case, topography played a significant role in the resultant deformation field and NTMs significantly underestimated the amplitude of surface displacement by up to 18% and 57% for the vertical and horizontal component of displacement, respectively. Maximum vertical components of displacement were mainly confined to steep slopes whereas maximum horizontal values occurred down-slope from these areas. At island volcanoes, the effect of topography was found to be very significant where some of the resultant deformation pattern was occurring in offshore areas, highlighting that at island volcanoes the entire topographic extent should be considered for deformation analyses as deformation does not stop at the coastline. Monitoring submerged volcanic flanks is challenging, however,

21699356, 2025, 8, Downloaded from https://agupubs.onlinelibrary.wiley.com/doi/10.1029/2024JB030805 by Karlsruher Institut für Technologie, Wiley Online Library on [02/09/2025]. See the Terms and Conditions (https://onlinelibrary.wiley.com/terms-and-conditions) on Wiley Online Library for rules of use; OA articles are governed by the applicable Creative Commons License

with improving technology, the possibility of monitoring these areas is becoming more achievable. Our method offers a tool that could enhance the design of geodetic networks and we encourage the use of topography in all marine volcano deformation modeling cases.

Data Availability Statement

The open-source software *Distmesh* is found at: http://persson.berkeley.edu/distmesh/. The open-source software *Triangular Dislocation* is found at: https://volcanodeformation.com/software. The implementation of the software is available at: https://oceanrep.geomar.de/id/eprint/61508/ (Campbell et al., 2024b). The data generated are available at: https://hdl.handle.net/20.500.12085/c1c2a749-7db4-43c7-81be-b1c02d4bbfca (Campbell et al., 2024a).

Acknowledgments
We thank Elisa Klein for the discussions on geomorphometric parameters and for providing the delineations for the case study volcanoes. We also thank Dr. Mehdi Nikkhoo for the helpful exchange regarding the modeling software and domains, and, Dr. Lorenzo Mantiloni for aiding in understanding mesh construction. Funding was provided by the Helmholtz Association's Initiative and Networking Fund (Young Investigator Group Grant VH-NG-1617) and this project has received funding from the European Research Council (ERC) under the European Union's Horizon 2020 research and innovation programme (grant agreement No. 948797). Open Access funding enabled and organized by Projekt DEAL.

References

Acocella, V., Puglisi, G., & Amelung, F. (2013). Flank instability at Mt. Etna. *Journal of Volcanology and Geothermal Research*, *251*, 1–4. (Flank instability at Mt. Etna). https://doi.org/10.1016/j.jvolgeores.2012.12.011

Azzaro, R., Bonforte, A., Branca, S., & Guglielmino, F. (2013). Geometry and kinematics of the fault systems controlling the unstable flank of Etna volcano (Sicily). *Journal of Volcanology and Geothermal Research*, *251*, 5–15. https://doi.org/10.1016/j.jvolgeores.2012.10.001

Battaglia, M., Cervelli, P. F., & Murray, J. R. (2013). dMODELS: A MATLAB software package for modeling crustal deformation near active faults and volcanic centers. *Journal of Volcanology and Geothermal Research*, *254*, 1–4. https://doi.org/10.1016/j.jvolgeores.2012.12.018

Biggs, J., & Wright, T. J. (2020). How satellite InSAR has grown from opportunistic science to routine monitoring over the last decade. *Nature Communications*, *11*(3863), 3863. https://doi.org/10.1038/s41467-020-17587-6

Bonaccorso, A. (2001). Mt. Etna volcano: Modelling of ground deformation patterns of recent eruptions and considerations on the associated precursors. *Journal of Volcanology and Geothermal Research*, *109*(1), 99–108. https://doi.org/10.1016/S0377-0273(00)00306-1

Bonaccorso, A., Currenti, G., & Del Negro, C. (2013). Interaction of volcano-tectonic fault with magma storage, intrusion and flank instability: A thirty years study at Mt. Etna volcano. *Journal of Volcanology and Geothermal Research*, *251*, 127–136. (Flank instability at Mt. Etna). https://doi.org/10.1016/j.jvolgeores.2012.06.002

Brown, R. L. (1975). *A dislocation approach to plate interaction* Doctoral dissertation. Massachusetts Institute of Technology. Retrieved from http://hdl.handle.net/1721.1/33237

Bruno, V., Aloisi, M., Gambino, S., Mattia, M., Ferlito, C., & Rossi, M. (2022). The most intense deflation of the last two decades at Mt. Etna: The 2019–2021 evolution of ground deformation and modeled pressure sources. *Geophysical Research Letters*, *49*(6), e2021GL095195. https://doi.org/10.1029/2021GL095195

Campbell, M., Furst, S., & Urlaub, M. (2024a). Calculated asymmetry and steepness parameters for onshore-only edifice portions and resultant displacement components calculated from analytical models [Dataset]. *GEOMAR Helmholtz Centre for Ocean Research Kiel*. Retrieved from https://hdl.handle.net/20.500.12085/c1c2a749-7db4-43c7-81be-b1c02d4bbfca

Campbell, M., Furst, S., & Urlaub, M. (2024b). VolcTopoDeformation [Software]. *GEOMAR Centre for Ocean Research Kiel*. https://doi.org/10.3289/SW_10_2024

Carracedo, J. C., Torrado, F. P., González, A. R., Soler, V., Fernandez-Turiel, J. L., Troll, V. R., & Wiesmaier, S. (2012). The 2011 submarine volcanic eruption in El Hierro (Canary Islands). *Geology Today*, *28*(2), 53–58. https://doi.org/10.1111/j.1365-2451.2012.00827.x

Casalbore, D., Romagnoli, C., Chiocci, F., & Frezza, V. (2010). Morpho-sedimentary characteristics of the volcaniclastic apron around Stromboli volcano (Italy). *Marine Geology*, *269*(3), 132–148. https://doi.org/10.1016/j.margeo.2010.01.004

Cayol, V., & Cornet, F. H. (1998). Effects of topography on the interpretation of the deformation field of prominent volcanoes—Application to Etna. *Geophysical Research Letters*, *25*(11), 1979–1982. https://doi.org/10.1029/98GL51512

Chadwick, W. W., Nooner, S. L., Zumberge, M. A., Embley, R. W., & Fox, C. G. (2006). Vertical deformation monitoring at axial seamount since its 1998 eruption using deep-sea pressure sensors. *Journal of Volcanology and Geothermal Research*, *150*(1), 313–327. (The Changing Shapes of Active Volcanoes). https://doi.org/10.1016/j.jvolgeores.2005.07.006

Chadwick, W. W., Wilcock, W. S. D., Nooner, S. L., Beeson, J. W., Sawyer, A. M., & Lau, T.-K. (2022). Geodetic monitoring at axial seamount since its 2015 eruption reveals a waning magma supply and tightly linked rates of deformation and seismicity. *Geochemistry, Geophysics, Geosystems*, *23*(1), e2021GC010153. https://doi.org/10.1029/2021GC010153

Comninou, M., & Dundurs, J. (1975). The angular dislocation in a half-space. *Journal of Elasticity*, *5*(3–4), 203–216. https://doi.org/10.1007/bf00126985

Crozier, J., Karlstrom, L., Montgomery-Brown, E., Angarita, M., Cayol, V., Bato, M. G., et al. (2023). Understanding the drivers of volcano deformation through geodetic model verification and validation. *Bulletin of Volcanology*, *85*(74), 74. https://doi.org/10.1007/s00445-023-01687-4

Currenti, G., Del Negro, C., Ganci, G., & Scandura, D. (2008). 3d numerical deformation model of the intrusive event forerunning the 2001 Etna eruption. *Physics of the Earth and Planetary Interiors*, *168*(1), 88–96. https://doi.org/10.1016/j.pepi.2008.05.004

Davis, P. M. (1986). Surface deformation due to inflation of an arbitrarily oriented triaxial ellipsoidal cavity in an elastic half-space, with reference to Kilauea volcano, Hawaii. *Journal of Geophysical Research*, *91*(B7), 7429–7438. https://doi.org/10.1029/JB091iB07p07429

Del Negro, C., Currenti, G., & Scandura, D. (2009). Temperature-dependent viscoelastic modeling of ground deformation: Application to Etna volcano during the 1993–1997 inflation period. *Physics of the Earth and Planetary Interiors*, *172*(3–4), 299–309. https://doi.org/10.1016/j.pepi.2008.10.019

Di Traglia, F., Battaglia, M., Nolesini, T., Lagomarsino, D., & Casagli, N. (2015). Shifts in the eruptive styles at Stromboli in 2010–2014 revealed by ground-based InSAR data. *Scientific Reports*, *5*(1), 13569. https://doi.org/10.1038/srep13569

Di Traglia, F., De Luca, C., Manzo, M., Nolesini, T., Casagli, N., Lanari, R., & Casu, F. (2021). Joint exploitation of space-borne and ground-based multitemporal InSAR measurements for volcano monitoring: The Stromboli volcano case study. *Remote Sensing of Environment*, *260*, 112441. https://doi.org/10.1016/j.rse.2021.112441

Di Traglia, F., Nolesini, T., Intrieri, E., Mugnai, F., Leva, D., Rosi, M., & Casagli, N. (2014). Review of ten years of volcano deformations recorded by the ground-based InSAR monitoring system at Stromboli volcano: A tool to mitigate volcano flank dynamics and intense volcanic activity. *Earth-Science Reviews*, *139*, 317–335. https://doi.org/10.1016/j.earscirev.2014.09.011

Fialko, Y., Khazan, Y., & Simons, M. (2001). Deformation due to a pressurized horizontal circular crack in an elastic half-space, with applications to volcano geodesy. *Geophysical Journal International*, *146*(1), 181–190. https://doi.org/10.1046/j.1365-246X.2001.00452.x

Furst, S., Urlaub, M., Klein, E., & Bonanati, C. (2023). Are eruptions reliable precursors to marine volcano collapses? *Frontiers in Earth Science*, *11*, 1130561. https://doi.org/10.3389/feart.2023.1130561

González, P. J., Samsonov, S. V., Pepe, S., Tiampo, K. F., Tizzani, P., Casu, F., et al. (2013). Magma storage and migration associated with the 2011–2012 El Hierro eruption: Implications for crustal magmatic systems at oceanic island volcanoes. *Journal of Geophysical Research: Solid Earth*, *118*(8), 4361–4377. https://doi.org/10.1002/jgrb.50289

Hager, B. H., King, R. W., & Murray, M. H. (1991). Measurement of crustal deformation using the global positioning system. *Annual Review of Earth and Planetary Sciences*, *19*(1), 351–382. https://doi.org/10.1146/annurev.ea.19.050191.002031

Head, M., Hickey, J., Gottsmann, J., & Fournier, N. (2019). The influence of viscoelastic crustal rheologies on volcanic ground deformation: Insights from models of pressure and volume change. *Journal of Geophysical Research: Solid Earth*, *124*(8), 8127–8146. https://doi.org/10.1029/2019JB017832

Hickey, J., & Gottsmann, J. (2014). Benchmarking and developing numerical finite element models of volcanic deformation. *Journal of Volcanology and Geothermal Research*, *280*, 126–130. https://doi.org/10.1016/j.jvolgeores.2014.05.011

Hickey, J., Pascal, K., Syers, R., & Alshembari, R. (2024). Topographical effects on volcano deformation signal intensity: Implications for GPS network configuration. *Geophysical Research Letters*, *51*(12), e2024GL108812. https://doi.org/10.1029/2024GL108812

Isken, M., Karstens, J., Nomikou, P., Parks, M. M., Drouin, V., Rivalta, E., et al. (2025). Volcanic crisis reveals coupled magma system at Santorini and Kolumbo. *Nature*. (accepted).

Johnson, J. H., Poland, M. P., Anderson, K. R., & Biggs, J. (2019). A cautionary tale of topography and tilt from Kīlauea Caldera. *Geophysical Research Letters*, *46*(8), 4221–4229. https://doi.org/10.1029/2018GL081757

Klein, E., Hadré, E., Krastel, S., & Urlaub, M. (2023). An evaluation of the general bathymetric chart of the ocean in shoreline-crossing geomorphometric investigations of volcanic islands. *Frontiers in Marine Science*, *10*, 2296–7745. https://doi.org/10.3389/fmars.2023.1259262

Kuriyama, K., & Mizuta, Y. (1993). Three-dimensional elastic analysis by the displacement discontinuity method with boundary division into triangular leaf elements. *International Journal of Rock Mechanics and Mining Sciences & Geomechanics Abstracts*, *30*(2), 111–123. https://doi.org/10.1016/0148-9062(93)90704-H

Lisowski, M. (2007). Analytical volcano deformation source models. In *Volcano deformation* (pp. 279–304). Springer Berlin Heidelberg. https://doi.org/10.1007/978-3-540-49302-0_8

López, C., Blanco, M. J., Abella, R., Brenes, B., Cabrera Rodríguez, V. M., Casas, B., et al. (2012). Monitoring the volcanic unrest of El Hierro (Canary Islands) before the onset of the 2011–2012 submarine eruption. *Geophysical Research Letters*, *39*(13). https://doi.org/10.1029/2012GL051846

Lungarini, L., Troise, C., Meo, M., & Natale, G. D. (2005). Finite element modelling of topographic effects on elastic ground deformation at Mt. Etna. *Journal of Volcanology and Geothermal Research*, *144*(1–4), 257–271. https://doi.org/10.1016/j.jvolgeores.2004.11.031

Maerten, F., Resor, P., Pollard, D., & Maerten, L. (2005). Inverting for slip on three-dimensional fault surfaces using angular dislocations. *Bulletin of the Seismological Society of America*, *95*(5), 1654–1665. https://doi.org/10.1785/0120030181

Mantiloni, L., Rivalta, E., & Davis, T. (2023). Mechanical modeling of pre-eruptive magma propagation scenarios at calderas. *Journal of Geophysical Research: Solid Earth*, *128*(3), e2022JB025956. https://doi.org/10.1029/2022JB025956

Martí, J., Pinel, V., Lõpez, C., Geyer, A., Abella, R., Tárraga, M., et al. (2013). Causes and mechanisms of the 2011–2012 El Hierro (Canary Islands) submarine eruption. *Journal of Geophysical Research: Solid Earth*, *118*(3), 823–839. https://doi.org/10.1002/jgrb.50087

McCormack Kilbride, B., Edmonds, M., & Biggs, J. (2016). Observing eruptions of gas-rich compressible magmas from space. *Nature Communications*, *7*(13744), 13744. https://doi.org/10.1038/ncomms13744

McTigue, D. F. (1987). Elastic stress and deformation near a finite spherical magma body: Resolution of the point source paradox. *Journal of Geophysical Research*, *92*(B12), 12931–12940. https://doi.org/10.1029/JB092iB12p12931

Mogi, K. (1958). Relations between the eruptions of various volcanoes and the deformation of the ground surfaces around them. *Bulletin of the Earthquake Research Institute*, *36*.

Montgomery-Brown, E. K., Segall, P., & Miklius, A. (2009). Kilauea slow slip events: Identification, source inversions, and relation to seismicity. *Journal of Geophysical Research*, *114*(B6). https://doi.org/10.1029/2008jb006074

Newman, A. V., Dixon, T. H., Ofoegbu, G. I., & Dixon, J. E. (2001). Geodetic and seismic constraints on recent activity at Long Valley Caldera, California: Evidence for viscoelastic rheology. *Journal of Volcanology and Geothermal Research*, *105*(3), 183–206. https://doi.org/10.1016/s0377-0273(00)00255-9

Nikkhoo, M. (2019). *Analytical and numerical elastic dislocation models of volcano deformation processes* Doctoral dissertation. University of Potsdam. https://doi.org/10.25932/publishup-42972

Nikkhoo, M., & Walter, T. R. (2015). Triangular dislocation: An analytical, artefact-free solution. *Geophysical Journal International*, *201*(2), 1119–1141. https://doi.org/10.1093/gji/ggv035

Palano, M., Puglisi, G., & Gresta, S. (2008). Ground deformation patterns at Mt. Etna from 1993 to 2000 from joint use of InSAR and GPS techniques. *Journal of Volcanology and Geothermal Research*, *169*(3), 99–120. https://doi.org/10.1016/j.jvolgeores.2007.08.014

Patanè, D., Barberi, G., De Gori, P., Cocina, O., Zuccarello, L., Garcia-Yeguas, A., et al. (2017). The shallow magma chamber of Stromboli Volcano (Italy). *Geophysical Research Letters*, *44*(13), 6589–6596. https://doi.org/10.1002/2017GL073008

Persson, P.-O., & Strang, G. (2004). A simple mesh generator in MATLAB. *Society for Industrial and Applied Mathematics*, *46*(2), 329–345. https://doi.org/10.1137/S0036144503429121

Petrone, C., Mollo, S., Gertisser, R. E. A., Buret, Y., Scarlato, P., Del Bello, E., et al. (2022). Magma recharge and mush rejuvenation drive paroxysmal activity at Stromboli volcano. *Nature Communications*, *13*(1), 7717. https://doi.org/10.1038/s41467-022-35405-z

Ronchin, E., Geyer, A., & Martí, J. (2015). Evaluating topographic effects on ground deformation: Insights from finite element modeling. *Surveys in Geophysics*, *36*(4), 513–548. https://doi.org/10.1007/s10712-015-9325-3

Ryan, W. B. F., Carbotte, S. M., Coplan, J. O., O'Hara, S., Melkonian, A., Arko, R., et al. (2009). Global multi-resolution topography synthesis. *Geochemistry, Geophysics, Geosystems*, *10*(3). https://doi.org/10.1029/2008GC002332

Salzer, J. T., Nikkhoo, M., Walter, T. R., Sudhaus, H., Reyes-Dávila, G., Bretón, M., & Arámbula, R. (2014). Satellite radar data reveal short-term pre-explosive displacements and a complex conduit system at Volcán de Colima, Mexico. *Frontiers in Earth Science*, *2*. https://doi.org/10.3389/feart.2014.00012

Segall, P. (2010). *Earthquake and volcano deformation*. Princeton University Press.

21699356, 2025, 8, Downloaded from https://agupubs.onlinelibrary.wiley.com/doi/10.1029/2024JB030805 by Karlsruher Institut für Technologie, Wiley Online Library on [02/09/2025]. See the Terms and Conditions (https://onlinelibrary.wiley.com/terms-and-conditions) on Wiley Online Library for rules of use; OA articles are governed by the applicable Creative Commons License

Simons, M., & Rosen, P. A. (2015). Interferometric synthetic aperture radar geodesy. In *Treatise on geophysics* (pp. 339–385). Elsevier.
Smith, J. R., Malahoff, A., & Shor, A. N. (1999). Submarine geology of the Hilina slump and morpho-structural evolution of Kilauea volcano, Hawaii. *Journal of Volcanology and Geothermal Research*, *94*(1), 59–88. https://doi.org/10.1016/S0377-0273(99)00098-0
Syamsidik, B., Luthfi, M., Suppasri, A., & Comfort, L. K. (2020). The 22 December 2018 Mount Anak Krakatau volcanogenic tsunami on Sunda strait coasts, Indonesia: Tsunami and damage characteristics. *Natural Hazards and Earth System Sciences*, *20*(2), 549–565. https://doi.org/10.5194/nhess-20-549-2020
Trasatti, E., Giunchi, C., & Bonafede, M. (2003). Effects of topography and rheological layering on ground deformation in volcanic regions. *Journal of Volcanology and Geothermal Research*, *122*(1–2), 89–110. https://doi.org/10.1016/S0377-0273(02)00473-0
Urlaub, M., Geersen, J., Petersen, F., Gross, F., Bonforte, A., Krastel, S., & Kopp, H. (2022). The submarine boundaries of Mount Etna's unstable southeastern flank. *Frontiers in Earth Science*, *10*, 810790. https://doi.org/10.3389/feart.2022.810790
Urlaub, M., Petersen, F., Gross, F., Bonforte, A., Puglisi, G., Guglielmino, F., et al. (2018). Gravitational collapse of Mount Etna's southeastern flank. *Science Advances*, *4*(10), 9700. https://doi.org/10.1126/sciadv.aat9700
van Wees, R. M., O'Hara, D., Kereszturi, G., Grosse, P., Lahitte, P., Tournigand, P.-Y., & Kervyn, M. (2024). Towards more consistent volcano morphometry datasets: Assessing boundary delineation and DEM impact on geometric and drainage parameters. *Geomorphology*, *465*, 109381. https://doi.org/10.1016/j.geomorph.2024.109381
Viccaro, M., Cannata, A., Cannavò, F., De Rosa, R., Giuffrida, M., Nicotra, E., et al. (2021). Shallow conduit dynamics fuel the unexpected paroxysms of Stromboli volcano during the summer 2019. *Scientific Reports*, *266*(1), 266. https://doi.org/10.1038/s41598-020-79558-7
Williams, C. A., & Wadge, G. (1998). The effects of topography on magma chamber deformation models: Application to Mt. Etna and radar interferometry. *Geophysical Research Letters*, *25*(10), 1549–1552. https://doi.org/10.1029/98GL01136
Williams, C. A., & Wadge, G. (2000). An accurate and efficient method for including the effects of topography in three-dimensional elastic models of ground deformation with applications to radar interferometry. *Journal of Geophysical Research*, *105*(B4), 8103–8120. https://doi.org/10.1029/1999jb900307
Yang, X., Davis, P. M., & Dieterich, J. H. (1988). Deformation from inflation of a dipping finite prolate spheroid in an elastic half-space as a model for volcanic stressing. *Journal of Geophysical Research*, *93*, 4249–4257. https://doi.org/10.1002/9781118782064.ch12
Yoffe, E. H. (1960). The angular dislocation. *Philosophical Magazine*, *5*(50), 161–175. https://doi.org/10.1080/14786436008243299

21699356, 2025, 8, Downloaded from https://agupubs.onlinelibrary.wiley.com/doi/10.1029/2024JB030805 by Karlsruher Institut für Technologie, Wiley Online Library on [02/09/2025]. See the Terms and Conditions (https://onlinelibrary.wiley.com/terms-and-conditions) on Wiley Online Library for rules of use; OA articles are governed by the applicable Creative Commons License